SCIENCE ADVANCES | RESEARCH ARTICLE

GEOCHEMISTRY

Highly oxidized intraplate basalts and deep carbon storage

Xu-Han Dong[1], Shui-Jiong Wang[1,2]*, Wenzhong Wang[3,4,5]*, Shichun Huang[6], Qiu-Li Li[7], Chengshuai Liu[8], Ting Gao[8], Shuguang Li[1], Shitou Wu[7]

Deep carbon cycle is crucial for mantle dynamics and maintaining Earth's habitability. Recycled carbonates are a strong oxidant in mantle carbon-iron redox reactions, leading to the formation of highly oxidized mantle domains and deep carbon storage. Here we report high $Fe^{3+}/\sum Fe$ values in Cenozoic intraplate basalts from eastern China, which are correlated with geochemical and isotopic compositions that point to a common role of carbonated melt with recycled carbonate signatures. We propose that the source of these highly oxidized basalts has been oxidized by carbonated melts derived from the stagnant subducted slab in the mantle transition zone. Diamonds formed during the carbon-iron redox reaction were separated from the melt due to density differences. This would leave a large amount of carbon (about four times of preindustrial atmospheric carbon budget) stored in the deep mantle and isolated from global carbon cycle. As such, the amounts of subducted slabs stagnated at mantle transition zone can be an important factor regulating the climate.

INTRODUCTION

The mantle oxidation state plays a crucial role in shaping our Earth, both its solid interior and atmosphere. In an isochemical mantle, the redox state decreases with increasing depth (*1*). However, this simple relationship can be disrupted by crustal recycling (*2*). For instance, deeply sourced, incompatible element enriched intraplate basalts, such as ocean island basalts (OIB), are more oxidized than mid-ocean ridge basalts (MORB) that sample the shallow depleted mantle (*2*–*4*). The presence of high-$Fe^{3+}/\sum Fe$ (up to 0.85) inclusions trapped within superdeep diamonds (*5*, *6*) also hints for highly oxidized deep (>250 km) mantle domains formed by carbon-iron redox reaction (*7*, *8*). However, the exact role of the proposed carbon-iron redox reaction in the petrogenesis of highly oxidized intraplate basalts remains to be explored.

The Pacific slab is subducting westward along the Japan-Izu-Bonin-Mariana arc (Fig. 1B) (*9*). Seismic tomography reveals that the subducted Pacific slab is now stagnated horizontally at the mantle transition zone (MTZ) beneath eastern China (EC), extending up to 1600 km west of the subduction zone. The mantle region above the stagnated subducted Pacific slab is referred to as the big mantle wedge (BMW) (*10*), which has been fully developed since early Cretaceous (*11*, *12*). The widespread, voluminous Cenozoic intraplate volcanism (~79,000 km^2) in EC is thus not associated with mantle plumes or arcs (Fig. 1, A and B) (*13*–*15*). Rather, they are related to partial melting of the BMW beneath EC triggered by fluids/melts released from the subducted Pacific slab stagnated at MTZ, during which subducted marine carbonates and carbonated oceanic crust may have played a key role (*13*–*16*).

The intraplate basalts from EC range from nephelinite to basaltic andesite in a total alkali versus silica diagram (fig. S1 and section S1 for materials). In a primitive mantle (PM)–normalized trace element diagram, the EC basalts have trace element patterns like OIB with HIMU (high μ, $\mu = {}^{238}U/{}^{204}Pb$) affinity (Fig. 1C) (*17*). Their ${}^{206}Pb/{}^{204}Pb$ ratios range from 16.6 to 19.0, lower than typical HIMU basalts, suggesting a young recycled oceanic component in the source (*13*).

Here, we measured the bulk rock $Fe^{3+}/\sum Fe$ and olivine $\delta^{18}O$ values in 42 well-studied Cenozoic intraplate basalts from EC. The studied Cenozoic EC basalts have $Fe^{3+}/\sum Fe$ values up to 0.6, much higher than those observed in MORB (0.14 ± 0.01; 1σ) (*18*) and OIB (from 0.16 to 0.4) (*19*, *20*). The high $Fe^{3+}/\sum Fe$ values are well correlated with olivine $\delta^{18}O$ values and vanadium-to-scandium (V/Sc) ratios, as well as bulk rock elemental and stable isotopic characteristics that are best explained as a result of carbon-iron redox reaction involving carbonated melts from subducted slab at the MTZ. We also used first-principles molecular dynamic calculations to constrain the melt diamond density crossover in the mantle. We found that during carbon-iron redox reaction, diamonds are denser than melts and, consequently, can be efficiently separated from the melts due to density difference. This reaction has facilitated deep carbon storage at the MTZ and formed a highly oxidized mantle endmember (HOME) which contributes substantially to intraplate basalts.

RESULTS

The $Fe^{3+}/\sum Fe$ ratios of EC basalts are unusually high, ranging from 0.11 to 0.6. Duplicate wet chemistry $Fe^{3+}/\sum Fe$ measurements of individual samples agree with each other within ±3% [relative standard deviation (RSD)] (table S1). The U.S. Geological Survey basalt standards BCR-2 and BHVO-2, and the Chinese national igneous rock standard GSR-1, GSR-2, and GSR-3 measured as unknowns yield $Fe^{3+}/\sum Fe$ values of 0.21, 0.25, 0.48, 0.47, and 0.38, respectively, consistent with their certified values within ±10% (table S2). A subset of samples covering the entire range of $Fe^{3+}/\sum Fe$ were analyzed

---

[1]State Key Laboratory of Geological Processes and Mineral Resources, China University of Geosciences (Beijing), Beijing 100083, China. [2]Frontiers Science Center for Deep-time Digital Earth, China University of Geosciences (Beijing), Beijing 100083, China. [3]School of Earth and Space Sciences, University of Science and Technology of China, Hefei 230026, China. [4]CAS Center for Excellence in Comparative Planetology, USTC, Hefei, China. [5]National Geophysical Observatory at Mengcheng, USTC, Mengcheng, China. [6]Department of Earth, Environmental, and Planetary Sciences, University of Tennessee, Knoxville, TN 37996-1410, USA. [7]State Key Laboratory of Lithospheric Evolution, Institute of Geology and Geophysics, Chinese Academy of Sciences, Beijing 100029, China. [8]State Key Laboratory of Environmental Geochemistry, Institute of Geochemistry, Chinese Academy of Sciences, Guiyang 550081, China.
*Corresponding author. Email: wsj@cugb.edu.cn (S.-J.W.); wwz@ustc.edu.cn (W.W.)

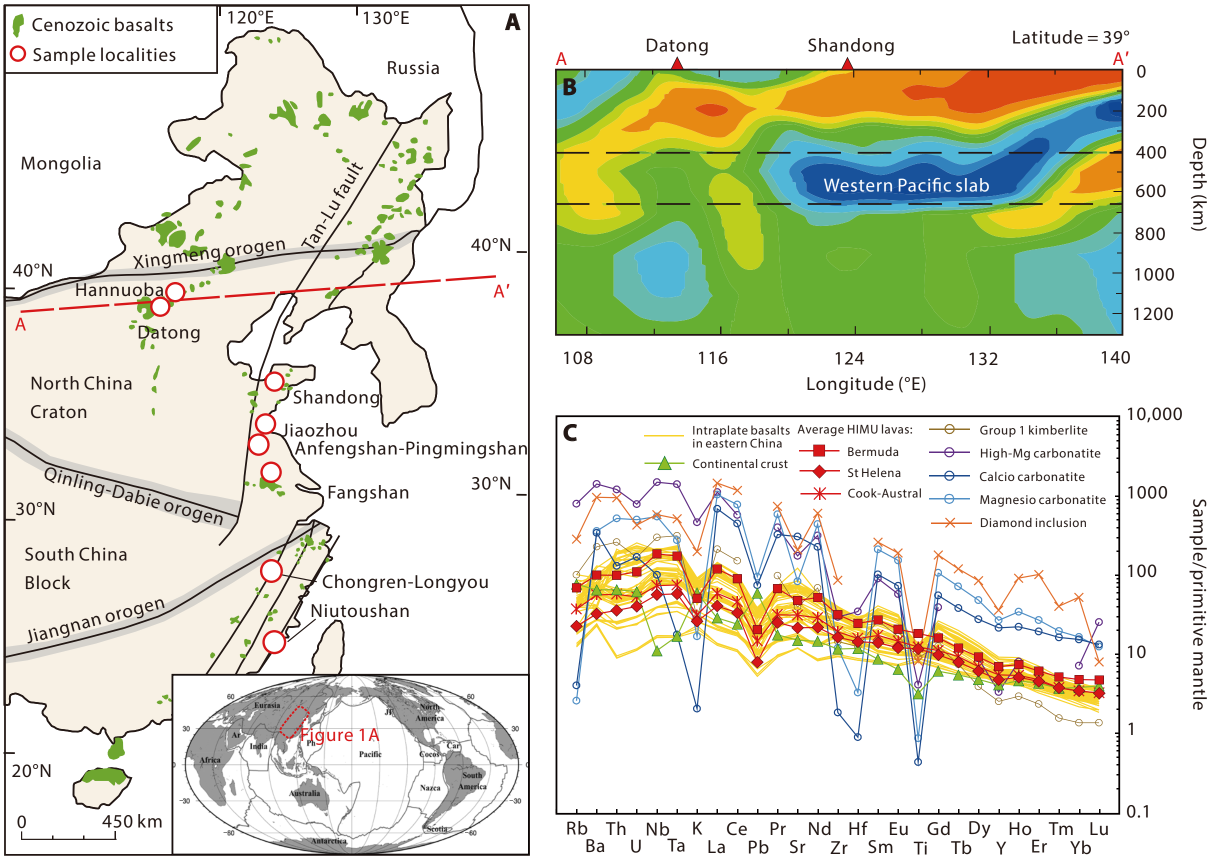

Fig. 1. Geological and geochemical background of Cenozoic intraplate basalts from EC. (**A**) Simplified geological map of EC and the distribution of Cenozoic intraplate basalts. (**B**) Stagnant Pacific slab beneath EC revealed by seismic tomography along the A-A′ profile, modified from Huang and Zhao (*9*). (**C**) Primitive mantle (PM) (*69*) normalized incompatible element diagram for EC Cenozoic basalts (yellow patterns), compared with OIB with HIMU (high μ, μ = $^{238}U/^{204}Pb$) affinity, continental crust, and carbonatite. Bermuda HIMU lavas are from Mazza *et al.* (*49*). The averages of other HIMU (St Helena and Cook-Austral) lavas are compiled from GEOROC (Geochemistry of Rocks of the Oceans and Continents) dataset (see data source in data file S1). The average of continental crust is from Rudnick and Gao (*70*). The deep diamond inclusion (11-ON-ZIZ) with HIMU-like incompatible trace elemental signatures is from Huang *et al.* (*5*). The averages of group 1 kimberlite and high-Mg carbonatite are from Weiss *et al.* (*71*). The averages of calcio and magnesio carbonatites are from Hoernle *et al.* (*72*).

using Mössbauer spectroscopy [fig. S2 for Mössbauer spectra (MBS)], and the Mössbauer results agree well with the wet chemical $Fe^{3+}/\sum Fe$ within ±10% (Fig. 2A).

Measured $\delta^{18}O$ values of phenocrystic olivines in EC basalts (from +5.2 to +4.2‰) are slightly lower than or comparable to the upper mantle estimate (+5.5 ± 0.2‰) (*21*). The V/Sc ratios of olivines vary from 0.88 to 2.27 (table S4), systematically lower than the average of PM (V/Sc = 4.9) (*22*). No intragrain variations in $\delta^{18}O$, V, or Sc were observed (fig. S3). The olivine-$\delta^{18}O$ and V/Sc are well correlated with the bulk rock $Fe^{3+}/\sum Fe$ values, with high-$Fe^{3+}/\sum Fe$ samples having higher $\delta^{18}O$ and lower V/Sc ratios (Fig. 2, B and C).

DISCUSSION

High $Fe^{3+}/\sum Fe$ of EC basalt

There are several shallow processes that could potentially affect the bulk rock $Fe^{3+}/\sum Fe$. We assess the effect of these processes below and provide compelling evidence that the high $Fe^{3+}/\sum Fe$ of the EC basalts reflect the mantle source signature.

In a few samples, alteration is visible as evidenced by the iddingsitization of olivines and elevated loss of ignition (LOI). These samples have $Fe^{3+}/\sum Fe$ values similar to samples without iddingsites from the same locality (fig. S5), suggesting that low-temperature iddingsite alteration of olivine has a negligible effect on the bulk rock $Fe^{3+}/\sum Fe$. The absence of a correlation between $Fe^{3+}/\sum Fe$ and LOI (fig. S5) further indicates that the high bulk rock $Fe^{3+}/\sum Fe$ is not controlled by surface alteration.

Crustal contamination is negligible in EC basalts (*14*, *15*), as indicated by the absence of positive Pb and negative Nb-Ta anomalies in trace element patterns (Fig. 1C). In plots of $Fe^{3+}/\sum Fe$ versus Sr and Nd isotopes (fig. S6), the enriched samples with low $\varepsilon_{Nd(i)}$ and high $^{87}Sr/^{88}Sr_i$ values tend to have lower $Fe^{3+}/\sum Fe$ values, suggesting that crustal contamination (if any) is unlikely responsible for the high $Fe^{3+}/\sum Fe$ values observed in EC basalts.

The presence of olivine and in rare cases pyroxene phenocrysts in the groundmass of EC basalts suggests that magmas have experienced crystal fractionation of olivine and pyroxene. Iron oxides are only found in groundmass in all samples, consistent with the high bulk rock MgO contents of EC basalts (MgO > 6 wt %; Fig. 2D).

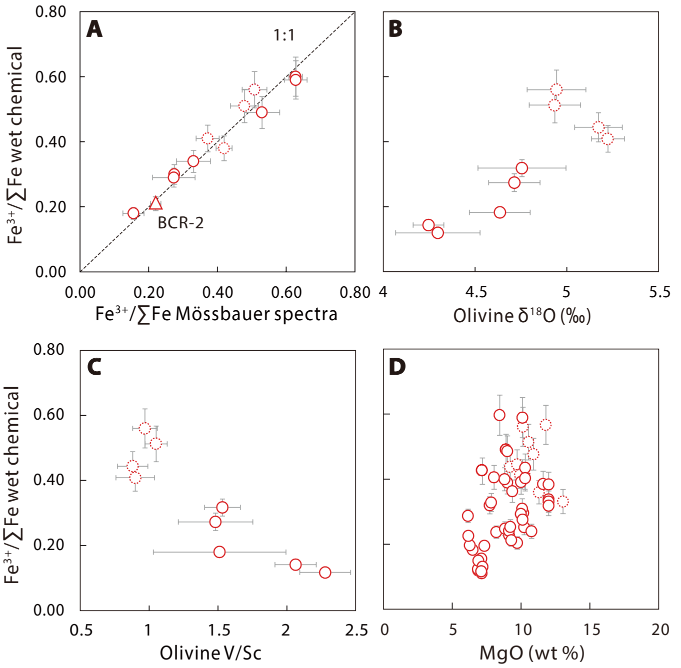

Fig. 2. $Fe^{3+}/\sum Fe$ values of Cenozoic intraplate basalts from EC. Wet chemistry $Fe^{3+}/\sum Fe$ values versus MBS $Fe^{3+}/\sum Fe$ values (**A**), olivine $\delta^{18}O$ (**B**), olivine V/Sc (**C**), and MgO (**D**). Wet chemistry and MBS $Fe^{3+}/\sum Fe$ values are reported in tables S1 and S3, respectively. The triangle represents the U.S. Geological Survey basalt standard BCR-2. Error bars in (A) reflect ±10% error for wet chemistry $Fe^{3+}/\sum Fe$ values and 1 SD for MBS $Fe^{3+}/\sum Fe$ values. Olivine $\delta^{18}O$ and V/Sc data are reported in table S4. Data points represent the average of analyzed olivine grains from individual EC basalts. A histogram plot of all analyzed olivine $\delta^{18}O$ ($n = 198$) and a plot of $\delta^{18}O$ versus V/Sc for all analyzed olivine grains are shown in fig. S4. Error bars in (B) and (C) represent 2 SE for olivine $\delta^{18}O$ and V/Sc of individual samples. Samples with LOI > 3 wt % are shown in red dashed.

Crystallization of olivine and pyroxene has a limited effect on the bulk rock $Fe^{3+}/\sum Fe$ (*23–25*). Specifically, a 2% decrease of MgO leads to a 0.01 increase in melt $Fe^{3+}/\sum Fe$ (*25*). This inference is consistent with the lack of a correlation between MgO and $Fe^{3+}/\sum Fe$ ($R^2 = 0.27$) in the investigated EC basalts (Fig. 2D). To eliminate the possible effect of crystal fractionation or crystal accumulation, the $Fe^{3+}/\sum Fe$ data were corrected by adding or subtracting equilibrium olivine until bulk rock reaches $Mg\#_{melt} = 0.72$ or 0.63, which corresponds to equilibrium with Fo_{90} or Fo_{85} olivines. The maximum correction for $Fe^{3+}/\sum Fe$ is less than 0.08 (section S2 and fig. S7), which is comparable to the analytical uncertainty.

Since Fe^{3+} is more incompatible than Fe^{2+} during mantle partial melting (*26*), melts are expected to have higher $Fe^{3+}/\sum Fe$ relative to their sources. For example, global MORB and OIB have higher $Fe^{3+}/\sum Fe$ than the normal mantle value of 0.036 (*2*, *4*, *18*, *27*, *28*). However, a recent study observed a constant $Fe^{3+}/\sum Fe$ value over variable degrees of partial melting (*25*). Our partial melting calculation also shows that melting of a normal mantle source can only produce melts with $Fe^{3+}/\sum Fe$ about 0.07 higher at most relative to the source (section S3 and fig. S8).

Magma degassing can cause a variation in $Fe^{3+}/\sum Fe$ (*20*). Hydrogen loss as H_2 may increase $Fe^{3+}/\sum Fe$ in the magma, but direct measurement of degassing volcanoes shows that H_2 is a minor component in degassed species compared to the more abundant oxidized species dominated by H_2O, CO_2, and SO_2 (*29*). While H_2O and CO_2 degassing has negligible effects on the $Fe^{3+}/\sum Fe$ of magma, sulfur degassing could potentially change the redox state of the degassed magma (*2*, *30–32*). Degassing of moderately reduced melts can decrease bulk rock $Fe^{3+}/\sum Fe$, with six moles of Fe^{3+} being reduced to Fe^{2+} for every mole of S^{2-} degassed as SO_2 (*20*). In contrast, degassing of oxidized melts can increase bulk rock $Fe^{3+}/\sum Fe$ (*30*, *33*), if sulfur in forms of $SO_4{}^{2-}$ was reduced to SO_2 by oxidizing the Fe^{2+} to Fe^{3+}. Because of the lack of information on the sulfur species in both magmas and gasses during the eruption of the EC basalts, the effect of sulfur degassing on the redox change of the degassed magma is difficult to constrain. Nevertheless, to evaluate the possible oxidizing effect caused by degassing of SO_2 for subaerial volcanoes, we assume that the magma with a total FeO of 12 wt % and $Fe^{3+}/\sum Fe$ of 0.25 has an initial sulfur content of 2500 parts per million in forms of sulfate and experiences 95% degassing to SO_2. This oxidized degassing scenario could elevate the $Fe^{3+}/\sum Fe$ of a degassed magma by 0.1 at most. Therefore, sulfur degassing alone cannot explain the observed high $Fe^{3+}/\sum Fe$ of the EC basalts.

Collectively, although all the above-mentioned shallow processes may have modified the $Fe^{3+}/\sum Fe$ in manners that we are unable to precisely constrain, the well-defined relationships between $Fe^{3+}/\sum Fe$ and key magmatic parameters, such as olivine $\delta^{18}O$ value and V/Sc ratio (Fig. 2, B and C), strongly suggest that the parent melts of EC basalts are highly oxidized. Olivine is the first mineral to crystallize from primitive basaltic magma during cooling, and thus, geochemical signatures preserved in olivine phenocrysts are less affected by late and posteruptive processes. Within olivine grains, the rim-core-rim analyses show uniform V, Sc, and $\delta^{18}O$ values (fig. S3), precluding the possible diffusion effect between olivine and melt. The V partitioning between olivine and melt is redox sensitive, with olivine formed in reduced magma having higher concentrations of V. In contrast, the partitioning of Sc between olivine and melt is redox insensitive. As such, the V/Sc in olivine phenocrysts records the magma redox state, with lower ratios deviating from the PM value (V/Sc = 4.9) (*22*) indicating more oxidizing conditions (*34*, *35*). The negative correlation between $Fe^{3+}/\sum Fe$ and olivine V/Sc ($R^2 = 0.81$; Fig. 2C) validates the utility of bulk rock $Fe^{3+}/\sum Fe$ as a redox proxy of primitive magma. In addition, the $Fe^{3+}/\sum Fe$ values are well correlated with a number of elemental and stable isotopic ratios (shown below) that are unaffected by magmatic or postemplacement processes (Figs. 3 and 4), further supporting that their highly oxidized nature is a source signature.

The nature of high $Fe^{3+}/\sum Fe$ endmember

The EC intraplate basalts are as oxidized as arc basalts with similar ranges in $Fe^{3+}/\sum Fe$; however, they show opposite $Fe^{3+}/\sum Fe$ versus Th/Ba and U/Pb trends (Fig. 3), implying different oxidation mechanisms. The highly oxidized nature of arc basalts is likely caused by the addition of slab-derived oxidizing fluids to the sub-arc mantle wedge source (*36*). A compilation of global arc basalt data shows that the high $Fe^{3+}/\sum Fe$ values are associated with low Th/Ba and U/Pb ratios (Fig. 3). This is a consequence of slab-derived fluid addition, because Ba and Pb are more mobile in fluid than Th and U (*37*). Conversely, the EC intraplate basalts have higher Th/Ba and U/Pb ratios which increase with $Fe^{3+}/\sum Fe$ values (Fig. 3). These correlations suggest that the oxidation of EC intraplate basalts is related to the stagnant Pacific slab that has preferentially lost fluid-mobile elements through dehydration processes during subduction.

Within EC intraplate basalts, high $Fe^{3+}/\sum Fe$ values are coupled with low Hf/Hf*, Ti/Ti*, and Zr/Nd and high CaO/Al_2O_3 (Fig. 4, A to D). Carbonated melts are characterized by high CaO/Al_2O_3 and extreme depletion of high field strength elements (such as Zr, Hf, and Ti) relative to rare earth elements (Fig. 1C) (*38*). The negative correlations of $Fe^{3+}/\sum Fe$ with Hf/Hf*, Ti/Ti*, and Zr/Nd and positive correlation of $Fe^{3+}/\sum Fe$ with CaO/Al_2O_3 thus indicate an essential role of a highly oxidized, carbonated endmember in the petrogenesis of EC basalts.

The Mg and Zn isotopic systematics further support that the carbonated melts may be derived from the subducted carbonated Pacific slab. Nearly all EC basalts exhibit higher $\delta^{66}Zn$ and lower $\delta^{26}Mg$ values compared to those of the PM or MORB (Fig. 4, E and F) (*16*, *39*). Given that Mg and Zn isotopes do not substantially fractionate during partial melting (*40*, *41*), the high $\delta^{66}Zn$ and low $\delta^{26}Mg$ signatures in EC basalts are best explained as a result of involving recycled carbonates that have distinctively lighter Mg and heavier Zn isotopic compositions ($\delta^{66}Zn$ up to +1.7‰; $\delta^{26}Mg$ down to −5‰; see fig. S9 for a compilation of Mg and Zn isotopic compositions of sedimentary carbonates) in the mantle sources of EC basalts (*16*, *39*). High-pressure high-temperature experiments suggest that subducted carbonated oceanic crust partially melts at the MTZ depth (*42*) and produces carbonated melts with high-$\delta^{66}Zn$ and low-$\delta^{26}Mg$ signatures of marine carbonates (*16*, *39*). The Pacific plate experienced a prolonged carbonation (*43*), and the altered oceanic crust recovered from the ODP Hole 801C contains ~1 wt % CO_2 on average (*44*). Subsequent low-degree melting of the subducted carbonated oceanic crust at the MTZ would preferentially consume carbonate minerals at the onset of melting to form carbonated melts (*42*). To account for the Zn and Mg isotopic composition of the carbonated melt endmember, mass balance predicts that during low-degree melting of the subducted carbonated oceanic crust, carbonate minerals in forms of dolomite or magnesite contributed as high as 10 to 20% in the melting reactions (section S4 for modeling details and fig. S10). Although it is difficult to make a tight constraint on the carbonate contribution using only Mg and Zn isotopic systematics in EC basalts, the positive $Fe^{3+}/\sum Fe$ versus $\delta^{66}Zn$ trend and negative $Fe^{3+}/\sum Fe$ versus $\delta^{26}Mg$ trend reveal that the recycled carbonates have played an important role in oxidizing the mantle source of EC basalts.

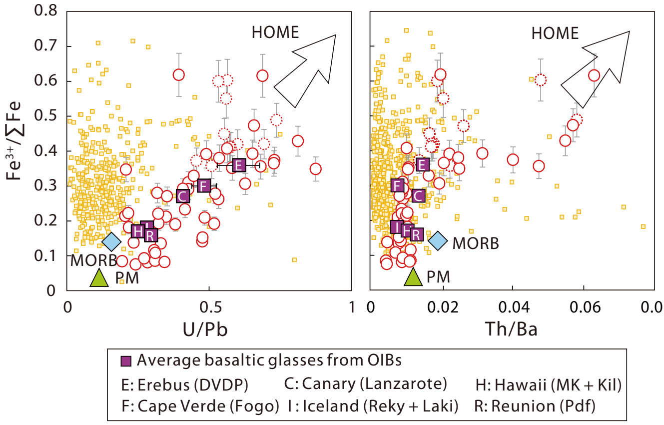

Fig. 3. Corrected $Fe^{3+}/\sum Fe$ values versus U/Pb and Th/Ba for Cenozoic intraplate basalts from EC. Data of EC Cenozoic intraplate basalts are shown in red circles and reported in table S1, with those with LOI > 3 wt % shown in red dashed. $Fe^{3+}/\sum Fe$ values are corrected for olivine crystal fractionation or accumulation. Error bars represent ±10% for $Fe^{3+}/\sum Fe$ values of EC Cenozoic intraplate basalts. Data of arc basalts are shown in yellow squares and provided in data file S2. The "most parental" $Fe^{3+}/\sum Fe$ values of OIB from each hotspot location are compiled from Brounce *et al.* (*19*) and Moussallam *et al.* (*2*). A complete data source including $Fe^{3+}/\sum Fe$ and average elemental compositions of OIB is provided in data file S3. Error bars represent 2 SE for OIB averages. The average $Fe^{3+}/\sum Fe$ values of MORB and PM are from Zhang *et al.* (*18*) and Canil *et al.* (*28*), respectively. The trace element compositions of average MORB and PM are from McDonough and Sun (*69*). HOME, highly oxidized mantle endmember.

Since low Hf/Hf*, Ti/Ti*, and Zr/Nd and high U/Pb, Th/Ba, and CaO/Al_2O_3 are typical characteristics of the HIMU endmember (*5*, *45*), the high-$Fe^{3+}/\sum Fe$ endmember of EC basalts may be a highly oxidized HIMU-like mantle endmember, which is related to carbonated melts originated from the stagnant Pacific slab at the MTZ beneath EC. We define this endmember as HOME. Consistent with this argument, the compositions of EC Cenozoic intraplate basalts in plots involving $Fe^{3+}/\sum Fe$ point toward the HIMU-type high-$Fe^{3+}/\sum Fe$ (0.85) diamond inclusion (Fig. 4, A to D), whose petrogenesis is related to partial melting of carbonated MORB at MTZ (*5*). In addition, the OIB averages also plot along the EC Cenozoic intraplate basalt trends (Figs. 3 and 4, A to D), implying that HOME may be widely sampled by global OIB as well (*2*).

Olivine-$\delta^{18}O$ values in EC basalts are also correlated with the above-mentioned bulk rock geochemical indices (Fig. 5). The hypothetical HOME is inferred to have mantle-like to higher olivine-$\delta^{18}O$ values, consistent with its carbonated origin (*46*). The low-$\delta^{18}O$ endmember may be related to the subcontinental lithospheric mantle, which has experienced extensive metasomatism by fluid/melts derived from hydrothermally altered subducted oceanic crust (*47*). Consistent with this inference, the metasomatized mantle xenolith PIC (Phlogopite-Ilmenite-Clinopyroxene) has a light O isotopic composition, located at the low-$\delta^{18}O$ endmember in the trends shown in Fig. 5 (*46*). A recent olivine-$\delta^{18}O$ investigation of global kimberlites from different cratons also shows that the metasomatized subcontinental lithospheric mantle is an important reservoir of isotopically light oxygen (*46*). Below, we focus on the HOME and discuss how it is produced using experimental results of carbon-iron redox reactions and first-principles simulations (see section S5 for computational details).

HOME produced by carbon-iron redox reaction

Mantle carbon-iron redox reaction can efficiently oxidize the mantle, in which Fe^{2+} is oxidized to Fe^{3+} by the reduction of carbonate to diamond. This reaction can be broken into two steps. First, disproportionation of Fe^{2+} ($3Fe^{2+} \rightarrow Fe^0 + 2Fe^{3+}$) occurs in the mantle below ~250 km depth (*7*, *48*). Second, carbonates in the deep upper mantle can be reduced to diamond by oxidizing metal Fe through a redox reaction of $2Fe^0 + C^{4+} \rightarrow 2Fe^{2+} + C^0$ (*7*). As such, the net reaction involving both carbonate and Fe^{2+} in silicates is $4Fe^{2+} + C^{4+} \rightarrow 4Fe^{3+} + C^0$, in which C^0 is formed as diamond because of high pressure.

This reaction may be favored in mantle domains where excess amount of carbonate is available, such as slab subduction and accumulation in the upper mantle and/or MTZ at places like BMW beneath EC (Fig. 1B). The subducted Paleo-Pacific slab may have penetrated into the lower mantle or consumed by ambient mantle, but the development of the BMW and slab stagnation in the MTZ since early Cretaceous have acted as a barrier for whole mantle convention (*11*, *12*).

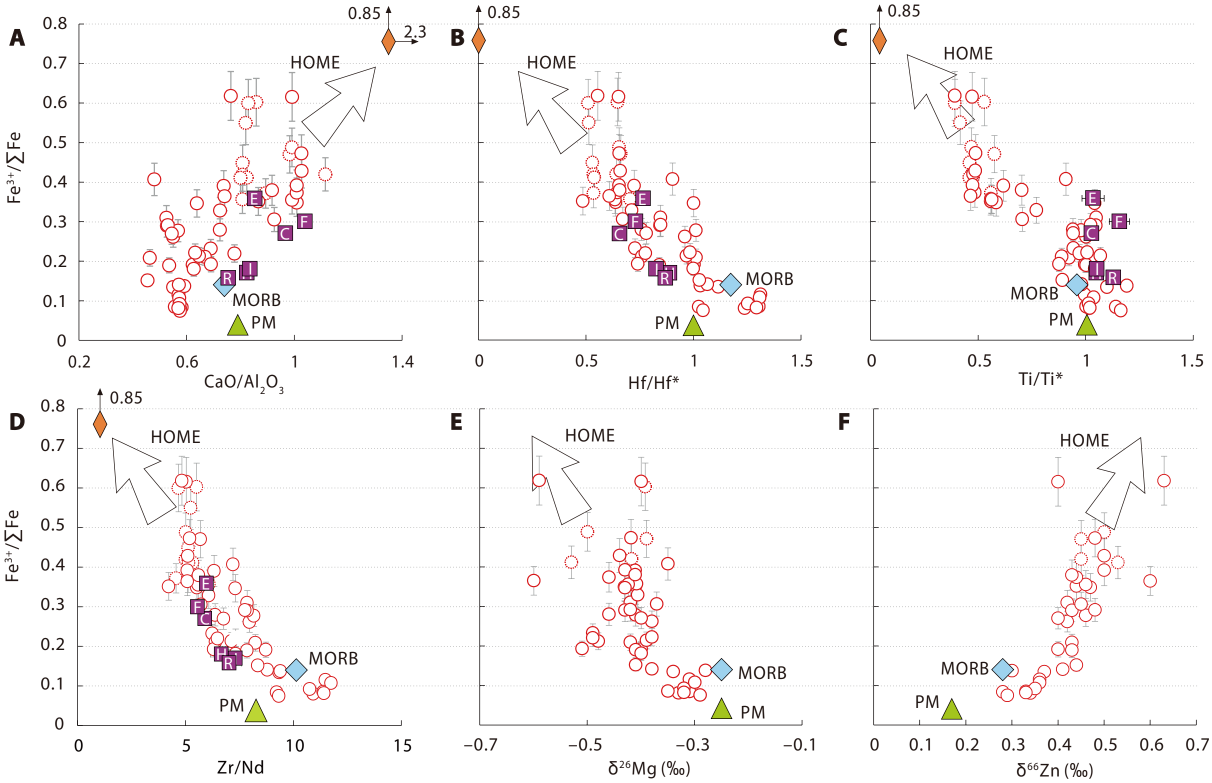

Fig. 4. Correlation between $Fe^{3+}/\sum Fe$ and recycled carbonate signatures for Cenozoic intraplate basalts from EC. Corrected $Fe^{3+}/\sum Fe$ values versus CaO/Al_2O_3 (**A**), Hf/Hf* (**B**), Ti/Ti* (**C**), Zr/Nd (**D**), $\delta^{26}Mg$ (**E**), and $\delta^{66}Zn$ (**F**). $Fe^{3+}/\sum Fe$ values are corrected for olivine crystal fractionation or accumulation. Legend and data source are same as Fig. 3. The orange diamond represents multiphase diamond inclusion (11-ON-ZIZ) from Huang *et al.* (*5*). $Hf/Hf^* = Hf_N/(Sm_N \times Nd_N)^{0.5}$; $Ti/Ti^* = Ti_N/(Nd_N{}^{-0.055} \times Sm_N{}^{0.333} \times Gd_N{}^{0.722})$; $\delta^{26}Mg = ({}^{26}Mg/{}^{24}Mg)_{sample}/({}^{26}Mg/{}^{24}Mg)_{DSM3} - 1) \times 1000$; $\delta^{66}Zn = ({}^{66}Zn/{}^{64}Zn)_{sample}/({}^{66}Zn/{}^{64}Zn)_{JMC\ 3\text{-}0749L} - 1) \times 1000$.

Another key for this reaction to occur toward right is to continuously remove the produced C^0 as diamond. To investigate the density difference between diamond and melts, we performed first-principles molecular dynamic simulations based on density functional theory to determine the melt diamond density crossover at mantle depths (see section S5 for computational details). We focused on three types of silicate melts, $Mg_6Ca_6Fe_5Si_{27}Al_{10}Na_3O_{88}$ (dry MORB), $Mg_6Ca_6Fe_5Si_{27}Al_{10}Na_3H_{18}O_{97}$ (MORB with 4.9 wt % water), and $Mg_6Ca_6Fe_5Si_{27}Al_{10}Na_3C_4O_{96}$ (MORB with 5.3 wt % CO_2) to model the effects of volatiles (tables S5 and S6). Our simulations together with previous studies show that diamond is always denser than silicate and carbonated melts at the bottom of upper mantle (~12 to 14 GPa). Because the density of melt decreases with increasing H_2O and CO_2 contents, the location of silicate/carbonated melt diamond density crossover could be even deeper if the melt is more volatile rich (Fig. 6A).

In summary, under the conditions of the lowermost upper mantle and the MTZ where redox reactions between Fe and C occur, diamond formed through this reaction would sink and be separated from the melts because of its high density. This would prompt the carbon-iron redox reaction toward right and leave a highly oxidized melt.

On the basis of above discussion, we propose that the formation of HOME is closely related to the carbonated melts produced by low-degree partial melting of the stagnant carbonated slabs at the MTZ beneath EC. These carbonated melts are expected to have low Hf/Hf*, Ti/Ti*, Zr/Nd, and $\delta^{26}Mg$ and high U/Pb, Th/Ba, CaO/Al_2O_3, and $\delta^{66}Zn$, characteristics of the HOME of EC basalts. Growth and separation of diamond from these carbonated melts as a result of the iron-carbon redox freezing reaction would have enriched the melts with Fe^{3+} (Fig. 6C). This mechanism is consistent with the traditional view that the HIMU endmember is partial melt of recycled ancient carbonated MORB (*5*, *49*, *50*). The highly oxidized carbonated melts could also react with and metasomatize the asthenospheric peridotite in the BMW. The outcome of this carbonated melt-peridotite interaction is twofold. First, the interaction progressively oxidizes the Fe^{2+} in peridotites to Fe^{3+} and reduces C^{4+} to form diamonds that are subsequently removed from the carbonated melt because of density difference. Second, metasomatism by carbonated melt leads to the low Hf/Hf*, Ti/Ti*, Zr/Nd, and $\delta^{26}Mg$ and high U/Pb, Th/Ba, CaO/Al_2O_3, and $\delta^{66}Zn$ signatures in the metasomatized peridotites. We envision that there is excess amount of CO_2 in the melt, so that the metasomatized peridotite can have a high $Fe^{3+}/\sum Fe$, and the remaining CO_2 will lower the solidus of the metasomatized peridotites (Fig. 6B), leading to low-degree partial melting that produces melts inherited the HOME signature (Fig. 6C). This mechanism is consistent with the alternative inference that the HIMU endmember is low-degree partial melt of carbonate-metasomatized peridotite (*45*).

Collectively, the uniquely high $Fe^{3+}/\sum Fe$ characteristics of EC basalts require that their mantle source(s) must be deep in the mantle (>300 km), within the pressure range that allows redox freezing reaction to happen, consistent with the most recent inference that the HIMU mantle source resides in the MTZ (*5*, *49*).

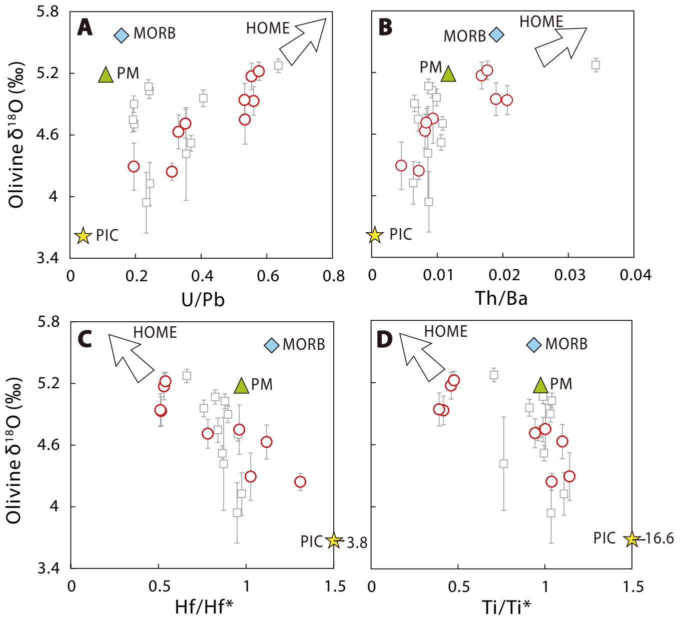

Fig. 5. Correlation between olivine $\delta^{18}O$ and bulk rock geochemical indices for Cenozoic intraplate basalts from EC. Olivine $\delta^{18}O$ values versus U/Pb (**A**), Th/Ba (**B**), Hf/Hf* (**C**), and Ti/Ti* (**D**). Data of EC Cenozoic intraplate basalts are reported in tables S1 and S4 and shown in red circle. Olivine $\delta^{18}O$ values of EC basalts from the literature (*47*) are shown in gray square. The $\delta^{18}O$ values of MORB and PM are from Valley *et al.* (*73*) and Mattey *et al.* (*21*), respectively. The trace element compositions of average MORB and PM are from McDonough and Sun (*69*). The $\delta^{18}O$ values and trace element compositions of PIC are from Xu *et al.* (*46*) and Fitzpayne *et al.* (*74*), respectively.

Averages of OIB form trends overlapping with the EC Cenozoic basalt trend, pointing toward the hypothetical HOME (Figs. 3 and 4, A to D). The HIMU-flavored basalts in general have higher $Fe^{3+}/\sum Fe$ than MORB (*2*), although not as high as those observed in EC intraplate basalts. The formation of HOME requires excess amounts of carbonates to oxidize all metal Fe in the mantle domains produced by Fe^{2+} disproportionation before converting Fe^{2+} to Fe^{3+}. The unique geological setting of the BMW beneath EC makes it possible. The long-term subduction and stagnancy of Pacific slab at the MTZ since early Cretaceous not only provide vast amounts of carbonates but also block mantle flow from the lower mantle that may be an infinite source for reduced metal Fe. It remains to be explored whether HOME is a common feature for all HIMU-type basalts, or it is only associated to and more prominent in specific geological settings, for example, the BMW developed at circum-Pacific subduction zones.

Deep carbon storage

The redox freezing reaction and the subsequent melt diamond separation would have resulted in the substantial storage of carbon within the deep mantle. The redox reaction of $4Fe^{2+} + C^{4+} \rightarrow 4Fe^{3+} + C^0$ can be used to estimate the overall quantity of carbon required for oxidizing the EC basalts and subsequently sequestering it from the global carbon cycle. The area of EC Cenozoic basalt can be determined by overlaying the distribution information of Cenozoic basalts on high-precision geomorphologic map, where the distribution information can be extracted by pixel from the geological map of EC using digital image processing program (*51*). The total area of EC Cenozoic basalts was estimated at about 79,000 km^2 (*51*). Assuming the layer thickness of the EC basalts is 10 km, 2400 gigatonne of carbon would be stored at the BMW to elevate the $Fe^{3+}/\sum Fe$ of EC basalts from a MORB-like value of 0.14 to an average value of 0.35 for the studied EC basalts (<50 Ma) (section S6 for modeling details and fig. S11), which is about four times the amount of

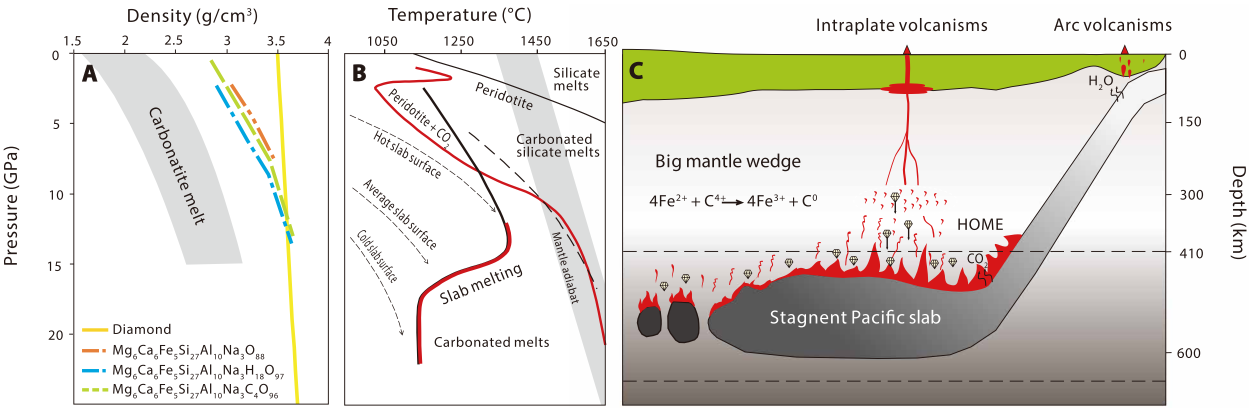

Fig. 6. Formation mechanism of HOME. (**A**) Density-pressure profiles of melts and diamond. Solid yellow: diamond; dashed orange: dry MORB ($Mg_6Ca_6Fe_5Si_{27}Al_{10}Na_3O_{88}$): dashed green: MORB with 4.9 wt % H_2O ($Mg_6Ca_6Fe_5Si_{27}Al_{10}Na_3H_{18}O_{97}$); dashed blue ($Mg_6Ca_6Fe_5Si_{27}Al_{10}Na_3C_4O_{96}$): MORB with 5.3 wt % CO_2. Data are reported in table S6. The density-pressure profiles of a variety of carbonate melts are from Massuyeau *et al.* (*75*). (**B**) The melting curves of carbonated MORB and carbonated peridotites compared to subduction geotherms and ambient mantle adiabat, modified from Thomson *et al.* (*42*) and Dasgupta (*76*). (**C**) Cartoon showing the formation of HOME in the BMW. Low-degree melting of stagnant carbonated Pacific slab generates carbonated melts. With excess C^{4+} replenished from subducted slabs, carbon-iron redox reaction happened in the melts ($4Fe^{2+} + C^{4+} \rightarrow 4Fe^{3+} + C^0$), and efficient separation of the newly formed diamond from the melts due to density difference would have elevated the melts' $Fe^{3+}/\sum Fe$, forming the HOME. These melts have HIMU elemental signatures, which subsequently metasomatizes the ambient peridotites. The interaction would have promoted carbon-iron redox reaction to precipitate diamond from melts and meanwhile elevate the $Fe^{3+}/\sum Fe$ of carbonated peridotites. Excess CO_2 from the subducted slab-derived carbonated melts decreases the solidus of metasomatized peridotites, leading to partial melting of the high-$Fe^{3+}/\sum Fe$ carbonate-metasomatized peridotitic domains to produce melts inherited the HOME signature.

preindustrial atmospheric carbon budget (590 gigatonne). The estimate entails several uncertainties. For instance, the total volume of Cenozoic intraplate basalts can vary substantially as its thickness is poorly constrained in many locations, and the measured $Fe^{3+}/\sum Fe$ do not represent the actual value of the parent melt considering the uncertainties from degassing and crystal fractionation. In addition, it is likely that the $Fe^{3+}/\sum Fe$ of melts could be decreased due to the reverse redox reaction ($4Fe^{3+} + C^0 \rightarrow 4Fe^{2+} + C^{4+}$) as the melts ascend and percolate across the redox melting frontline (~250 km) (*52*, *53*) and mix with the lithospheric mantle-derived melts. Nevertheless, we argue for a link between oxidized intraplate basalts and deep carbon storage, both of which may form from subducted slab stagnant at MTZ. Seismic images of the circum-Pacific reveal that the uppermost lower mantle (660 to 1000 km) is an important reservoir for the subducted slabs, forming BMW around the majority of the circum-Pacific (*54*). Therefore, the formation of HOME may not be restricted to BMW beneath EC. The possible climate effect of the deep carbon storage associated with the formation of the HOME in the geological history needs further investigations.

MATERIALS AND METHODS

Wet chemistry $Fe^{3+}/\Sigma Fe$ analysis

$Fe^{3+}/\Sigma Fe$ ratios were measured using redox titration with a potassium dichromate ($K_2Cr_2O_7$) solution at the Element Geochemistry Laboratory of the China University of Geosciences, Beijing (*55*). One hundred milligrams of sample powders was mixed with 5 ml of concentrated hydrofluoric acid and 10 ml 1:1 Milli-Q water:sulfuric acid (H_2SO_4) in teflon crucibles with lid. The mixtures were heated on a hotplate until they reached boiling temperature. After heating for another 10 min, the mixtures were complexed and buffered by 25 ml of boric acid (H_3BO_3) and 150 ml of Milli-Q water at room temperature. Fifteen milliliters of 3:7 H_3PO_4-H_2SO_4 mixture was added into the solutions before titration. Ferrous Fe was then titrated by 0.01 M $K_2Cr_2O_7$ with sodium diphenylamine sulfonate ($C_{12}H_{10}NSO_3Na$) as the indicator. We used the certified FeO value (FeO = 7.60 wt %) of rock standard GSR-3 to calibrate the potassium dichromate concentration. The $Fe^{3+}/\Sigma Fe$ was calculated as $(FeO_{total} - FeO)/FeO_{total}$. Five rock reference materials including BCR-2, BHVO-2, GSR-1, GSR-2, and GSR-3 were processed together with samples as unknowns. Their measured FeO contents agree with their reported certified values (*55*, *56*), with analytical uncertainties within ±10% in $Fe^{3+}/\Sigma Fe$ (table S2). The results of EC Cenozoic intraplate basalts are shown in table S1. Repeated analyses of FeO for a selected set of samples show good agreement between duplicates within ±10% (table S1).

MBS $Fe^{3+}/\Sigma Fe$ analysis

To verify the $Fe^{3+}/\Sigma Fe$ measured using wet chemistry, we performed Mössbauer spectroscopy to determine the $Fe^{3+}/\Sigma Fe$ of a subset of samples that cover the entire range of $Fe^{3+}/\Sigma Fe$. The MBS were collected and processed to identify Fe species with different oxidation states. The MBS were obtained using a Mössbauer spectrometer (MS-65, Science Engineering and Education Co., USA) with a high-velocity resolution (registered in 1024 channels) at ~12 K (cooled down by liquid helium, but the system was not able to reach 4.2 K due to the low power of the compressor) coupled with a SHI-850 cryogenic system from Janis Research Co. Inc. (Wilmington, MA) at the Institute of Geochemistry, Chinese Academy of Sciences. ^{57}Co in the Rh matrix provided ~14.4 eV gamma rays. Each sample of 20 to 40 mg was loaded in the Cu sample holder with a 1.0-cm-diameter window and a thickness as large as ~0.3 cm to accommodate any large-sized sample. The holder was entirely sealed with a Kapton tape. The precise weight of each sample is calculated to match the ideal absorber thickness, which optimizes the signal-to-noise ratio (*57*).

All measurements were performed in a velocity range of ±10 mm/s to ensure that any hyperfine split pattern (e.g., sextets) from magnetically ordered Fe-bearing phases was detected. The MBS reflects the nature and strength of the hyperfine interactions, whose key parameters consist of the isomer shift (IS), quadrupole splitting (QS or ε), and magnetic field (*T*). The velocity zero is defined as the center of the α-Fe calibration spectrum (e.g., at ~295 K). The IS is the velocity shift of the samples relative to the source and is expressed relative to the α-iron calibration spectrum, which can be used to identify the electronic structure of the atom and then give its valence and spinning state. The electric QS parameter (or ε) is a measure of the spatial distribution of electrons around the ^{57}Fe nucleus and is influenced by both asymmetry of valence electrons and longer-range contributions from the entire mineral lattice (*58*). The magnetic field (*T*) is used to measure the interaction between the nuclear magnetic moment and the net effective magnetic field on the nucleus. The collection time in the cryogenic measurements is approximately 3 to 4 days to improve precision. During cryogenic measurements, the temperature was kept below 11 K during data acquisition, which was detected at the He gas outflow port and on the sample holder mount. Data were collected over 512 channels, which on folding resulted in 256 channels. The raw data were folded to eliminate the geometric effect and then fitted using the least-square method with one or more appropriate sets of Lorentzian lines by 4.0Pre of the MossWinn program (http://mosswinn.com). The main fitting parameters include IS, magnetic field, and QS. The SD and chi-square (goodness of fit, χ^2) of all the parameters are calculated by 100 Monte Carlo iterations on MossWinn 4.0.

The relative areas of the individual components in the MBS can be considered as representing the amounts of Fe in the respective phases to a good approximation because the resonant fractions of the individual phases present in the samples do not differ largely (*59*). In this study, Fe^{2+}/Fe^{3+} was assessed using MBS collected at ~12 K. In the 12 K spectra, different spectral components of samples were resolved: (i) an Fe^{III} quadrupole doublet (e.g., 10FS10) or an Fe^{III} quadrupole doublet and an Fe^{III} sextet (e.g., 08LHS02); (ii) an Fe^{II} quadrupole doublet. All the parameters (e.g., IS) of these spectral components are shown in table S3. The MBS $Fe^{3+}/\Sigma Fe$ data agree with the wet chemistry $Fe^{3+}/\Sigma Fe$ within ±10% (Fig. 2A), further confirming the accuracy of wet chemistry $Fe^{3+}/\Sigma Fe$ measurement of EC basalts.

In situ SIMS oxygen isotope analysis

We measured oxygen isotopic compositions of olivines at the Institute of Geology and Geophysics, Chinese Academy of Sciences (IGGCAS), Beijing, China. First, we drilled out the selected portions of the thin sections and mounted them together with the oxygen isotope reference material San Carlos olivine in epoxy resin. Then, sample mounts were polished and gold-coated. Oxygen isotopic ratios of olivine were analyzed using a CAMECA IMS-1280 multicollector ion probe. The Cs^+ primary beam was accelerated at 10 kV with an intensity of ~2 nA. The spot is approximately 20 μm in diameter (10-μm beam diameter + 10-μm raster). An electron gun was used to compensate for sample charging during the analysis. Secondary ions were extracted at a potential of −10 kV. Oxygen isotopes were measured in multicollector mode with two off-axis Faraday cups. Each analysis consisted of 20 cycles with 4-s counting time. We analyzed the reference material San Carlos olivine after analyzing every four unknown samples in the experiment to monitor analytical precision and calibrate instrumental mass fractionation. The average δ^{18}O value for San Carlos olivine is 5.23 ‰, with an external reproducibility (2 SD) of 0.38‰ in this study, which is similar to the reported certified value of 5.3 ‰ (*60*). Previous studies have demonstrated negligible matrix effect for olivine with Fo numbers > 70 (*61*). Secondary ion mass spectrometry (SIMS) oxygen isotope analysis on olivine with Fo number < 70 has significant instrumental mass fractionation (*61*–*65*). Therefore, only olivine grains with Fo number > 70 were selected for oxygen isotope analysis.

Laser ablation inductively coupled plasma mass spectrometry

After SIMS analyses, the gold coating was removed. We determined the elemental compositions of olivine using a GeolasHD 193 nm ArF excimer LA system (Coherent, Göttingen, Germany) coupled to an Element XR sector field–inductively coupled (ICP)–mass spectrometry (MS) (Thermo Fisher Scientific, Bremen, Germany) at the IGGCAS, Beijing, China. Helium was used as the carrier gas and mixed with Ar gas before being transported to the plasma torch. Olivines were analyzed at a laser repetition of 5 Hz, an energy density of 3 J/cm^2, and a spot size of 32 μm. The locations of the laser spots were selected on the basis of binocular microscopic and backscattered electron image examination to avoid any cracks and inclusions. Each spot was ablated for 40 s for ICP-MS measurement after 10 s of blank gas measurement, followed by 10 s of washout. Possible surface contamination was removed in a preablation step with three laser pulses before analysis. ARM-3 reference glass was used for the instrument- and time-dependent fractionations of Fe/Mg ratios and all minor-trace elements (*66*). Olivine standard reference materials (RM) MongOLSh11-2 and XEN were measured as unknown for data quality control. RM MongOLSh11-2 has average concentrations of 5.99 μg/g (2 SD = 0.39) for V and 3.7 μg/g (2 SD = 0.42) for Sc, and RM XEN has average concentrations of 2.09 μg/g (2 SD = 0.26) and 2.1 μg/g (2 SD = 0.4) for V and Sc, in agreement with the reported certified values (*67*, *68*). Each set of standard samples, including ARM-3, GOR132-G, MongOLSh11-2, and XEN, was analyzed once every 10 unknown samples were interspersed.

Supplementary Materials

This PDF file includes:
Supplementary Text
Figs. S1 to S11
Legends for tables S1 to S7
Legends for data files S1 to S3
References

Other Supplementary Material for this manuscript includes the following:
Tables S1 to S7
Data files S1 to S3

REFERENCES AND NOTES

1. D. J. Frost, C. A. McCammon, The redox state of Earth's mantle. *Annu. Rev. Earth Planet. Sci.* **36**, 389–420 (2008).
2. Y. Moussallam, M.-A. Longpré, C. McCammon, A. Gomez-Ulla, E. F. Rose-Koga, B. Scaillet, N. Peters, E. Gennaro, R. Paris, C. Oppenheimer, Mantle plumes are oxidised. *Earth Planet. Sci. Lett.* **527**, 115798 (2019).
3. Y. S. He, X. Meng, S. Ke, H. Wu, C. Zhu, F.-Z. Teng, J. Hoefs, J. Huang, W. Yang, L. Xu, Z. Hou, Z.-Y. Ren, S. Li, A nephelinitic component with unusual δ^{56}Fe in Cenozoic basalts from eastern China and its implications for deep oxygen cycle. *Earth Planet. Sci. Lett.* **512**, 175–183 (2019).
4. R. W. Nicklas, R. K. M. Hahn, L. N. Willhite, M. G. Jackson, V. Zanon, R. Arevalo, J. M. D. Day, Oxidized mantle sources of HIMU- and EM-type Ocean Island Basalts. *Chem. Geol.* **602**, 120901 (2022).
5. S. C. Huang, O. Tschauner, S. Y. Yang, M. Humayun, W. J. Liu, S. N. Gilbert Corder, H. A. Bechtel, J. Tischler, HIMU geochemical signature originating from the transition zone. *Earth Planet. Sci. Lett.* **542**, 116323 (2020).
6. E. S. Kiseeva, D. M. Vasiukov, B. J. Wood, C. McCammon, T. Stachel, M. Bykov, E. Bykova, A. Chumakov, V. Cerantola, J. W. Harris, L. Dubrovinsky, Oxidized iron in garnets from the mantle transition zone. *Nat. Geosci.* **11**, 144–147 (2018).
7. A. Rohrbach, M. W. Schmidt, Redox freezing and melting in the Earth's deep mantle resulting from carbon-iron redox coupling. *Nature* **472**, 209–212 (2011).
8. R. B. Tao, Y. W. Fei, Recycled calcium carbonate is an efficient oxidation agent under deep upper mantle conditions. *Commun. Earth Environ.* **2**, 45 (2021).
9. J. L. Huang, D. P. Zhao, High-resolution mantle tomography of China and surrounding regions. *J. Geophys. Res.* **111**, B09305 (2006).
10. E. Ohtani, D. Zhao, The role of water in the deep upper mantle and transition zone: Dehydration of stagnant slabs and its effects on the big mantle wedge. *Russ. Geol. Geophys.* **50**, 1073–1078 (2009).
11. S. G. Li, Y. Wang, Formation time of the big mantle wedge beneath eastern China and a new lithospheric thinning mechanism of the North China craton-Geodynamic effects of deep recycled carbon. *Sci. China Earth Sci.* **61**, 853–868 (2018).
12. Q. Ma, Y.-G. Xu, Magmatic perspective on subduction of Paleo-Pacific plate and initiation of big mantle wedge in East Asia. *Earth Sci. Rev.* **213**, 103473 (2021).
13. Y. Xu, H. Li, L. Hong, L. Ma, Q. Ma, M. Sun, Generation of Cenozoic intraplate basalts in the big mantle wedge under eastern Asia. *Sci. China Earth Sci.* **61**, 869–886 (2018).
14. R. Xu, Y. Liu, X.-C. Wang, S. F. Foley, Y. Zhang, H. Yuan, Generation of continental intraplate alkali basalts and implications for deep carbon cycle. *Earth Sci. Rev.* **201**, 103073 (2020).
15. G. Zeng, L. H. Chen, X. S. Xu, S. Y. Jiang, A. W. Hofmann, Carbonated mantle sources for Cenozoic intra-plate alkaline basalts in Shandong, North China. *Chem. Geol* **273**, 35–45 (2010).
16. S. G. Li, W. Yang, S. Ke, X. Meng, H. Tian, L. J. Xu, Y. S. He, J. Huang, X. C. Wang, Q. Xia, W. D. Sun, X. Y. Yang, Z. Y. Ren, H. Q. Wei, Y. S. Liu, F. C. Meng, J. Yan, Deep carbon cycles constrained by a large-scale mantle Mg isotope anomaly in eastern China. *Nat. Sci. Rev.* **4**, 111–120 (2017).
17. Y. Liu, S. Gao, P. B. Kelemen, W. Xu, Recycled crust controls contrasting source compositions of Mesozoic and Cenozoic basalts in the North China Craton. *Geochim. Cosmochim. Acta* **72**, 2349–2376 (2008).
18. H. L. Zhang, E. Cottrell, P. A. Solheid, K. A. Kelley, M. M. Hirschmann, Determination of Fe^{3+}/ΣFe of XANES basaltic glass standards by Mössbauer spectroscopy and its application to the oxidation state of iron in MORB. *Chem. Geol.* **479**, 166–175 (2018).
19. M. Brounce, E. Stolper, J. Eiler, The mantle source of basalts from Reunion Island is not more oxidized than the MORB source mantle. *Contrib. Mineral. Petrol.* **177**, 7 (2021).
20. Y. Moussallam, C. Oppenheimer, B. Scaillet, F. Gaillard, P. Kyle, N. Peters, M. Hartley, K. Berlo, A. Donovan, Tracking the changing oxidation state of Erebus magmas, from mantle to surface, driven by magma ascent and degassing. *Earth Planet. Sci. Lett.* **393**, 200–209 (2014).
21. D. Mattey, D. Lowry, C. Macpherson, Oxygen isotope composition of mantle peridotite. *Earth Planet. Sci. Lett.* **128**, 231–241 (1994).
22. C. T. A. Lee, W. P. Leeman, D. Canil, Z. X. A. Li, Similar V/Sc systematics in MORB and arc basalts: Implications for the oxygen fugacities of their mantle source regions. *J. Petrol.* **46**, 2313–2336 (2005).
23. K. A. Kelley, E. Cottrell, The influence of magmatic differentiation on the oxidation state of Fe in a basaltic arc magma. *Earth Planet. Sci. Lett.* **329**, 109–121 (2012).
24. O. Shorttle, Y. Moussallam, M. E. Hartley, J. Maclennan, M. Edmonds, B. J. Murton, Fe-XANES analyses of Reykjanes Ridge basalts: Implications for oceanic crust's role in the solid Earth oxygen cycle. *Earth Planet. Sci. Lett.* **427**, 272–285 (2015).
25. Y. Moussallam, G. Georgeais, E. F. Rose-Koga, K. T. Koga, M. E. Hartley, B. Scaillet, C. Oppenheimer, N. Peters, CO_2-undersaturated melt inclusions from the South West Indian Ridge record surprisingly uniform redox conditions. *Geochem. Geophys. Geosyst.* **24**, e2023GC011235 (2023).
26. G. A. Gaetani, The behavior of Fe^{3+}/∑Fe during partial melting of spinel lherzolite. *Geochim. Cosmochim. Acta* **185**, 64–77 (2016).
27. E. Cottrell, S. K. Birner, M. Brounce, F. A. Davis, L. E. Waters, K. A. Kelley, "Oxygen fugacity across tectonic settings" in *Magma Redox Geochemistry*, R. Moretti, D. R. Neuville, Eds. (Wiley, 2021), pp. 33–61.

28. D. Canil, H. S. C. O'Neill, D. G. Pearson, R. L. Rudnick, W. F. McDonough, D. A. Carswell, Ferric iron in peridotites and mantle oxidation-states. *Earth Planet. Sci. Lett.* **123**, 205–220 (1994).
29. Y. Moussallam, C. Oppenheimer, A. Aiuppa, G. Giudice, M. Moussallam, P. Kyle, Hydrogen emissions from Erebus volcano, Antarctica. *Bull. Volcanol.* **74**, 2109–2120 (2012).
30. F. Gaillard, B. Scaillet, M. Pichavant, G. Iacono-Marziano, The redox geodynamics linking basalts and their mantle sources through space and time. *Chem. Geol.* **418**, 217–233 (2015).
31. R. Moretti, D. R. Neuville, Eds. *Magma Redox Geochemistry* (American Geophysical Union, Wiley, 2021).
32. Y. Moussallam, M. Edmonds, B. Scaillet, N. Peters, E. Gennaro, I. Sides, C. Oppenheimer, The impact of degassing on the oxidation state of basaltic magmas: A case study of Kīlauea volcano. *Earth Planet. Sci. Lett.* **450**, 317–325 (2016).
33. S. Ding, T. Plank, P. J. Wallace, D. J. Rasmussen, Sulfur_X: A model of sulfur degassing during magma ascent. *Geochem. Geophys. Geosyst.* **24**, e2022GC010552 (2023).
34. D. Canil, Vanadium partitioning and the oxidation state of Archaean komatiite magmas. *Nature* **389**, 842–845 (1997).
35. S. F. Foley, D. Prelevic, T. Rehfeldt, D. E. Jacob, Minor and trace elements in olivines as probes into early igneous and mantle melting processes. *Earth Planet. Sci. Lett.* **363**, 181–191 (2013).
36. K. A. Kelley, E. Cottrell, Water and the oxidation state of subduction zone magmas. *Science* **325**, 605–607 (2009).
37. T. Kogiso, Y. Tatsumi, S. Nakano, Trace element transport during dehydration processes in the subducted oceanic crust: 1. Experiments and implications for the origin of ocean island basalts. *Earth Planet. Sci. Lett.* **148**, 193–205 (1997).
38. M. J. Walter, G. P. Bulanova, L. S. Armstrong, S. Keshav, J. D. Blundy, G. Gudfinnsson, O. T. Lord, A. R. Lennie, S. M. Clark, C. B. Smith, L. Gobbo, Primary carbonatite melt from deeply subducted oceanic crust. *Nature* **454**, 622–625 (2008).
39. S. A. Liu, Z. Z. Wang, S. G. Li, J. Huang, W. Yang, Zinc isotope evidence for a large-scale carbonated mantle beneath eastern China. *Earth Planet. Sci. Lett.* **444**, 169–178 (2016).
40. F. Moynier, D. Vance, T. Fujii, P. Savage, The isotope geochemistry of zinc and copper. *Rev. Miner. Geochem.* **82**, 543–600 (2017).
41. F. Teng, Z., Magnesium isotope geochemistry. *Rev. Mineral. Geochem.* **82**, 219–287 (2017).
42. A. R. Thomson, M. J. Walter, S. C. Kohn, R. A. Brooker, Slab melting as a barrier to deep carbon subduction. *Nature* **529**, 76–79 (2016).
43. M. A. Kendrick, J. X. Zhao, Y. X. Feng, Early accretion and prolonged carbonation of the Pacific Ocean's oldest crust. *Geology* **50**, 1270–1275 (2022).
44. J. C. Alt, D. A. H. Teagle, Hydrothermal alteration of upper oceanic crust formed at a fast-spreading ridge: Mineral, chemical, and isotopic evidence from ODP Site 801. *Chem. Geol.* **201**, 191–211 (2003).
45. Y. Weiss, C. Class, S. L. Goldstein, T. Hanyu, Key new pieces of the HIMU puzzle from olivines and diamond inclusions. *Nature* **537**, 666–670 (2016).
46. J. Y. Xu, A. Giuliani, Q. L. Li, K. Lu, J. C. Melgarejo, W. L. Griffin, Light oxygen isotopes in mantle-derived magmas reflect assimilation of sub-continental lithospheric mantle material. *Nat. Commun.* **12**, 6295 (2021).
47. X. C. Wang, S. A. Wilde, Q. L. Li, Y. N. Yang, Continental flood basalts derived from the hydrous mantle transition zone. *Nat. Commun.* **6**, 7700 (2015).
48. A. Rohrbach, C. Ballhaus, U. Golla-Schindler, P. Ulmer, V. S. Kamenetsky, D. V. Kuzmin, Metal saturation in the upper mantle. *Nature* **449**, 456–458 (2007).
49. S. E. Mazza, E. Gazel, M. Bizimis, R. Moucha, P. Beguelin, E. A. Johnson, R. J. McAleer, A. V. Sobolev, Sampling the volatile-rich transition zone beneath Bermuda. *Nature* **569**, 398–403 (2019).
50. P. R. Castillo, The recycling of marine carbonates and sources of HIMU and FOZO ocean island basalts. *Lithos* **216-217**, 254–263 (2015).
51. X. Y. Chen, L. H. Chen, Y. Chen, G. Zeng, J. Q. Liu, Distribution summary of Cenozoic basalts in Central and Eastern China. *Geol. J. China Univ.* **20**, 507–519 (2014).
52. V. Stagno, D. O. Ojwang, C. A. McCammon, D. J. Frost, The oxidation state of the mantle and the extraction of carbon from Earth's interior. *Nature* **493**, 84–88 (2013).
53. S. F. Foley, "Redox melting in the mantle" in *Magma Redox Geochemistry*, R. Moretti, D. R. Neuville, Eds. (Wiley, 2021), pp. 93–113.
54. Y. Fukao, M. Obayashi, Subducted slabs stagnant above, penetrating through, and trapped below the 660 km discontinuity. *J. Geophys. Res. Solid Earth* **118**, 5920–5938 (2013).
55. M. Yin, J. X. Li, Eds. *Analysis of Rock and Minerals* (Geological Publishing House, 2011), vol. 2, pp. 1–862.
56. P. A. Sossi, J. D. Foden, G. P. Halverson, Redox-controlled iron isotope fractionation during magmatic differentiation: An example from the Red Hill intrusion, S. Tasmania. *Contrib. Mineral. Petrol.* **164**, 757–772 (2012).
57. A. Kumar, M. R. Singh, P. R. Sarma, K. C. Tripathi, Optimised thickness of diffusive Mossbauer absorbers. *J. Phys. D Appl. Phys.* **22**, 465–466 (1989).
58. A. Thompson, D. G. Rancourt, O. A. Chadwick, J. Chorover, Iron solid-phase differentiation along a redox gradient in basaltic soils. *Geochim. Cosmochim. Acta* **75**, 119–133 (2011).
59. T. Mansfeldt, S. Schuth, W. Hausler, F. E. Wagner, S. Kaufhold, M. Overesch, Iron oxide mineralogy and stable iron isotope composition in a Gleysol with petrogleyic properties. *J. Soil Sedim.* **12**, 97–114 (2012).
60. J. M. Eiler, C. Graham, J. W. Valley, SIMS analysis of oxygen isotopes: Matrix effects in complex minerals and glasses. *Chem. Geol.* **138**, 221–244 (1997).
61. F. Guo, J. T. Guo, C. Y. Wang, W. M. Fan, C. W. Li, L. Zhao, H. X. Li, J. Y. Li, Formation of mafic magmas through lower crustal AFC processes - An example from the Jinan gabbroic intrusion in the North China Block. *Lithos* **179**, 157–174 (2013).
62. J. Eiler, E. M. Stolper, M. C. McCanta, Intra- and intercrystalline oxygen isotope variations in minerals from basalts and peridotites. *J. Petrol.* **52**, 1393–1413 (2011).
63. N. T. Kita, T. Ushikubo, B. Fu, M. J. Spicuzza, J. W. Valley, Analytical developments on oxygen three isotope analyses using a new generation ion microprobe IMS-1280, in *38th Lunar and Planetary science Conference*, Abstract 1981, 2007.
64. I. Bindeman, A. Gurenko, O. Sigmarsson, M. Chaussidon, Oxygen isotope heterogeneity and disequilibria of olivine crystals in large volume Holocene basalts from Iceland: Evidence for magmatic digestion and erosion of Pleistocene hyaloclastites. *Geochim. Cosmochim. Acta* **72**, 4397–4420 (2008).
65. A. A. Gurenko, I. N. Bindeman, M. Chaussidon, Oxygen isotope heterogeneity of the mantle beneath the Canary Islands: Insights from olivine phenocrysts. *Contrib. to Mineral. Petrol.* **162**, 349–363 (2011).
66. S. T. Wu, G. Wörner, K. P. Jochum, B. Stoll, K. Simon, A. Kronz, The preparation and preliminary characterisation of three synthetic andesite reference glass materials (ARM-1, ARM-2, ARM-3) for in situ microanalysis. *Geostand. Geoanal. Res.* **43**, 567–584 (2019).
67. V. G. Batanova, J. M. Thompson, L. V. Danyushevsky, M. V. Portnyagin, D. Garbe-Schonberg, E. Hauri, J. I. Kimura, Q. Chang, R. Senda, K. Goemann, C. Chauvel, S. Campillo, D. A. Ionov, A. V. Sobolev, New olivine reference material for in situ microanalysis. *Geostand. Geoanal. Res.* **43**, 453–473 (2019).
68. S. T. Wu, Y. D. Wu, Y. H. Yang, H. Wang, C. Huang, L. W. Xie, J. H. Yang, Simultaneous quantification of forsterite content and minor-trace elements in olivine by LA-ICP-MS and geological applications in Emeishan large igneous province. *Minerals-Basel* **10**, 634 (2020).
69. W. F. McDonough, S. S. Sun, The composition of the Earth. *Chem. Geol.* **120**, 223–253 (1995).
70. R. L. Rudnick, S. Gao, "Composition of the continental crust" in *Treatise on Geochemistry*, H. D. Holland, K. K. Turekian, Eds. (Pergamon, 2003), vol. 3, pp. 1–64.
71. Y. Weiss, W. L. Griffin, D. R. Bell, O. Navon, High-Mg carbonatitic melts in diamonds, kimberlites and the sub-continental lithosphere. *Earth Planet. Sci. Lett.* **309**, 337–347 (2011).
72. K. Hoernle, G. Tilton, M. J. Le Bas, S. Duggen, D. Garbe-Schönberg, Geochemistry of oceanic carbonatites compared with continental carbonatites: Mantle recycling of oceanic crustal carbonate. *Contrib. Mineral. Petrol.* **142**, 520–542 (2002).
73. J. W. Valley, M. J. Spicuzza, T. Ushikubo, Correlated δ^{18}O and [Ti] in lunar zircons: A terrestrial perspective for magma temperatures and water content on the Moon. *Contrib. Miner. Petrol.* **167**, 956 (2014).
74. A. Fitzpayne, A. Giuliani, J. Hergt, D. Phillips, P. Janney, New geochemical constraints on the origins of MARID and PIC rocks: Implications for mantle metasomatism and mantle-derived potassic magmatism. *Lithos* **318-319**, 478–493 (2018).
75. M. Massuyeau, X. Ritter, C. Sanchez-Valle, A density model for high-pressure carbonate-rich melts applied to carbonatitic magmatism in the upper mantle. *Chem. Geol.* **622**, 121275 (2022).
76. R. Dasgupta, Ingassing, storage, and outgassing of terrestrial carbon through geologic time. *Rev. Miner. Geochem.* **75**, 183–229 (2013).
77. Z. Z. Wang, S. A. Liu, Evolution of intraplate alkaline to tholeiitic basalts via interaction between carbonated melt and lithospheric mantle. *J. Petrol.* **62**, 1–25 (2021).
78. S. P. Qian, Z. Y. Ren, L. Zhang, L. B. Hong, J. Q. Liu, Chemical and Pb isotope composition of olivine-hosted melt inclusions from the Hannuoba basalts, North China Craton: Implications for petrogenesis and mantle source. *Chem. Geol.* **401**, 111–125 (2015).
79. G. Zeng, L. H. Chen, A. W. Hofmann, X. J. Wang, J. Q. Liu, X. Yu, L. W. Xie, Nephelinites in eastern China originating from the mantle transition zone. *Chem. Geol.* **576**, 120276 (2021).
80. J. Huang, S.-G. Li, Y. Xiao, S. Ke, W.-Y. Li, Y. Tian, Origin of low δ^{26}Mg Cenozoic basalts from South China Block and their geodynamic implications. *Geochim. Cosmochim. Acta* **164**, 298–317 (2015).
81. F. C. Meng, T. F. Li, H. M. Xue, F. L. Liu, Z. Q. Xu, Two serials of basic magmas from different mantle sources of Late Cretaceous in east Shandong province, China: A comparative study on basalts from Zhucheng and Jiaozhou. *Acta Petrol. Sin.* **22**, 1644–1656 (2006).
82. J. Yang, "Petrological and geochemical studies of the cenozoic basalts and hosted peridotite xenoliths in Zhejiang and Fujian provinces," thesis, China University of Geosciences (Beijing) (2015).
83. C. Q. Sun, J. Q. Liu, B. Xu, H. T. You, First radiocarbon dating of a Holocene eruption of the Datong volcanic field, eastern China. *J. Volcanol. Geotherm. Res.* **384**, 275–279 (2019).

84. H. Zhao, Z. Liu, C. M. Wang, S. H. Li, Luminescence dating of volcanic eruptions in Datong, northern China. *Quat. Geochronol.* **30**, 357–362 (2015).
85. D. Luo, L. H. Chen, G. Zeng, Genesis of intra-continental strongly alkaline volcanic rocks: A case study of Dashan nephelinites in Wudi, Shandong Province, North China. *Acta Petrol. Sin.* **25**, 311–319 (2009).
86. S. Z. Sheng, S. J. Wang, X. M. Yang, L. H. Chen, G. Zeng, Y. Xiao, J. Shen, X. H. Dong, Y. W. Lv, Sulfide dissolution on the nickel isotopic composition of basaltic rocks. *J. Geophys. Res. Solid Earth* **127**, e2022JB024555 (2022).
87. Z. Z. Wang, S. A. Liu, L. H. Chen, S. G. Li, G. Zeng, Compositional transition in natural alkaline lavas through silica-undersaturated melt–lithosphere interaction. *Geology* **46**, 771–774 (2018).
88. E. Cottrell, K. A. Kelley, The oxidation state of Fe in MORB glasses and the oxygen fugacity of the upper mantle. *Earth Planet. Sci. Lett.* **305**, 270–282 (2011).
89. P. A. Sossi, O. Nebel, J. Foden, Iron isotope systematics in planetary reservoirs. *Earth Planet. Sci. Lett.* **452**, 295–308 (2016).
90. P. L. Roeder, R. F. Emslie, Olivine-liquid equilibrium. *Mineral. Petrol.* **29**, 275–289 (1970).
91. A. D. T. Goode, Oxidation of natural olivines. *Nature* **248**, 500–501 (1974).
92. M. J. Walter, Melting of garnet peridotite and the origin of komatiite and depleted lithosphere. *J. Petrol.* **39**, 29–60 (1998).
93. J. Wang, F. Huang, X. Xiong, E. Takahashi, "*Partition Coefficients of Fe^{3+} and Fe^{2+} between Mantle Minerals and Melts: Implications for Redox Variations during Mantle Melting*" (AGU Fall Meeting 2021, New Orleans, LA, 2021).
94. R. Dasgupta, M. M. Hirschmann, The deep carbon cycle and melting in Earth's interior. *Earth Planet. Sci. Lett.* **298**, 1–13 (2010).
95. B. B. Karki, First-principles computation of mantle materials in crystalline and amorphous phases. *Phys. Earth Planet.* **240**, 43–69 (2015).
96. R. Wentzcovitch, Y. G. Yu, Z. Wu, Thermodynamic properties and phase relations in mantle minerals investigated by first principles Quasiharmonic theory. *Rev. Mineral. Geochem*. **71**, 59–98 (2010).
97. W. Wang, Y. Xu, D. Sun, S. Ni, R. Wentzcovitch, Z. Wu, Velocity and density characteristics of subducted oceanic crust and the origin of lower-mantle heterogeneities. *Nat. Commun.* **11**, 64 (2020).
98. R. Caracas, K. Hirose, R. Nomura, M. D. Ballmer, Melt–crystal density crossover in a deep magma ocean. *Earth Planet. Sci. Lett.* **516**, 202–211 (2019).
99. C. B. Agee, Crystal-liquid density inversions in terrestrial and lunar magmas. *Phys. Earth Planet. In.* **107**, 63–74 (1998).
100. J. W. E. Drewitt, M. J. Walter, J. P. Brodholt, J. M. R. Muir, O. T. Lord, Hydrous silicate melts and the deep mantle H_2O cycle. *Earth Planet. Sci. Lett.* **581**, 117408 (2022).
101. N. V. Solomatova, R. Caracas, Buoyancy and structure of volatile-rich silicate melts. *J. Geophys. Res. Solid Earth* **126**, e2020JB021045 (2021).
102. N. V. Solomatova, R. Caracas, C. E. Manning, Carbon sequestration during core formation implied by complex carbon polymerization. *Nat. Commun.* **10**, 789 (2019).
103. M. E. Hartley, O. Shorttle, J. Maclennan, Y. Moussallam, M. Edmonds, Olivine-hosted melt inclusions as an archive of redox heterogeneity in magmatic systems. *Earth Planet. Sci. Lett.* **479**, 192–205 (2017).
104. R. L. Helz, E. Cottrell, M. Brounce, K. A. Kelley, Olivine-melt relationships and syneruptive redox variations in the 1959 eruption of Kīlauea Volcano as revealed by XANES. *J. Volcanol. Geotherm. Res.* **333**, 1–14 (2017).
105. M. Brounce, E. Stolper, J. Eiler, Redox variations in Mauna Kea lavas, the oxygen fugacity of the Hawaiian plume, and the role of volcanic gases in Earth's oxygenation. *Proc. Natl. Acad. Sci. U.S.A.* **114**, 8997–9002 (2017).
106. M. Gaborieau, M. Laubier, N. Bolfan-Casanova, C. A. McCammon, D. Vantelon, A. I. Chumakov, F. Schiavi, D. R. Neuville, S. Venugopal, Determination of Fe^{3+}/ΣFe of olivine-hosted melt inclusions using Mössbauer and XANES spectroscopy. *Chem. Geol.* **547**, 119646 (2020).
107. B. G. Pokrovsky, V. Mavromatis, O. S. Pokrovsky, Co-variation of Mg and C isotopes in late Precambrian carbonates of the Siberian Platform: A new tool for tracing the change in weathering regime? *Chem. Geol.* **290**, 67–74 (2011).
108. A. Geske, J. Zorlu, D. K. Richter, D. Buhl, A. Niedermayr, A. Immenhauser, Impact of diagenesis and low grade metamorphosis on isotope (δ^{26}Mg, δ^{13}C, δ^{18}O and ^{87}Sr/^{86}Sr) and elemental (Ca, Mg, Mn, Fe and Sr) signatures of Triassic sabkha dolomites. *Chem. Geol.* **332-333**, 45–64 (2012).
109. J. A. Higgins, D. P. Schrag, Constraining magnesium cycling in marine sediments using magnesium isotopes. *Geochim. Cosmochim. Acta* **74**, 5039–5053 (2010).
110. J. A. Higgins, D. P. Schrag, The Mg isotopic composition of Cenozoic seawater- evidence for a link between Mg-clays, seawater Mg/Ca, and climate. *Earth Planet. Sci. Lett.* **416**, 73–81 (2015).
111. J. A. Higgins, D. P. Schrag, Records of Neogene seawater chemistry and diagenesis in deep-sea carbonate sediments and pore fluids. *Earth Planet. Sci. Lett.* **357**, 386–396 (2012).
112. M. S. Fantle, J. Higgins, The effects of diagenesis and dolomitization on Ca and Mg isotopes in marine platform carbonates: Implications for the geochemical cycles of Ca and Mg. *Geochim. Cosmochim. Acta* **142**, 458–481 (2014).
113. C. L. Blattler, N. R. Miller, J. A. Higgins, Mg and Ca isotope signatures of authigenic dolomite in siliceous deep-sea sediments. *Earth Planet. Sci. Lett.* **419**, 32–42 (2015).
114. S. Pichat, C. Douchet, F. Albarède, Zinc isotope variations in deep-sea carbonates from the eastern equatorial Pacific over the last 175 ka. *Earth Planet. Sci. Lett.* **210**, 167–178 (2003).
115. S. A. Liu, H. C. Wu, S. Z. Shen, G. Q. Jiang, S. H. Zhang, Y. W. Lv, H. Zhang, S. G. Li, Zinc isotope evidence for intensive magmatism immediately before the end-Permian mass extinction. *Geology* **45**, 343–346 (2017).
116. T. C. Sweere, A. J. Dickson, H. C. Jenkyns, D. Porcelli, M. Elrick, S. H. J. M. van den Boorn, G. M. Henderson, Isotopic evidence for changes in the zinc cycle during Oceanic Anoxic Event 2 (Late Cretaceous). *Geology* **46**, 463–466 (2018).
117. H. Chen, P. S. Savage, F.-Z. Teng, R. T. Helz, F. Moynier, Zinc isotope fractionation during magmatic differentiation and the isotopic composition of the bulk Earth. *Earth Planet. Sci. Lett.* **369-370**, 34–42 (2013).

Acknowledgments: We thank J. Huang and S. A. Liu for providing some of the intraplate basalt samples. We also thank H. Qin for help in the lab. **Funding:** The research was funded by the National Key R&D Program of China (2022YFF0801004), the National Nature Science Foundation of China (Grant 41973010), the National Key R&D Program of China (2019YFA0708404), and Fundamental Research Funds for the Central Universities (Grant 2652023001) to S.-J.W. W.W. acknowledges support from the Fundamental Research Funds for the Central Universities (WK2080000189). S.H. acknowledges support from NSF grant EAR-2244895. C.L. acknowledges support from the National Natural Science Foundation of China (42025705). **Author contributions:** S.-J.W. conceived and designed the project and provided funding. X.-H.D., S.-J.W., W.W., S.H., and S.L. contributed to the interpretation of the results, and X.-H.D., S.-J.W., W.W., and S.H. wrote and revised the manuscript. Q.-L.L. and S.W. provided olivine oxygen isotopes and trace element analysis. C.L. and T.G. provided MBS measurement. **Competing interests:** The authors declare that they have no competing interests. **Data and materials availability:** All data needed to evaluate the conclusions in the paper are present in the paper and/or the Supplementary Materials.

Submitted 7 November 2023
Accepted 28 June 2024
Published 7 August 2024
10.1126/sciadv.adm8138